



HAL
open science

An Experimental and Theoretical Investigation of the $C(1D) + N_2 \rightarrow C(3P) + N_2$ Quenching Reaction at Low Temperature

Kevin Hickson, Jean-Christophe J.-C. Loison, François Lique, Jacek Klos

► **To cite this version:**

Kevin Hickson, Jean-Christophe J.-C. Loison, François Lique, Jacek Klos. An Experimental and Theoretical Investigation of the $C(1D) + N_2 \rightarrow C(3P) + N_2$ Quenching Reaction at Low Temperature. *Journal of Physical Chemistry A*, 2016, 120 (16), pp.2504-2513. 10.1021/acs.jpca.6b00480 . hal-03105403

HAL Id: hal-03105403

<https://hal.science/hal-03105403>

Submitted on 11 Jan 2021

HAL is a multi-disciplinary open access archive for the deposit and dissemination of scientific research documents, whether they are published or not. The documents may come from teaching and research institutions in France or abroad, or from public or private research centers.

L'archive ouverte pluridisciplinaire **HAL**, est destinée au dépôt et à la diffusion de documents scientifiques de niveau recherche, publiés ou non, émanant des établissements d'enseignement et de recherche français ou étrangers, des laboratoires publics ou privés.

An Experimental and Theoretical Investigation of the $C(^1D) + N_2 \rightarrow C(^3P) + N_2$ Quenching Reaction at Low Temperature

Kevin M. Hickson,^{1,2} Jean-Christophe Loison,^{1,2} François Lique³ and Jacek Kłos^{4*}*

¹Université de Bordeaux, Institut des Sciences Moléculaires, UMR 5255, F-33400 Talence,
France

²CNRS, Institut des Sciences Moléculaires, UMR 5255, F-33400 Talence, France

³LOMC - UMR 6294, CNRS-Université du Havre, 25 rue Philippe Lebon, BP 1123, 76063 Le
Havre, France

⁴Department of Chemistry and Biochemistry, University of Maryland, College Park, Maryland
20742-2021 USA

Abstract

The gas-phase quenching reaction $C(^1D) + N_2 \rightarrow C(^3P) + N_2$ has been investigated experimentally over the temperature range 50 - 296 K using a supersonic flow reactor. $C(^1D)$ atoms were produced in-situ by the pulsed multiphoton dissociation of CBr_4 precursor molecules. Rate constants for this process were measured using a chemical tracer method whereby the $C(^1D)$

+ H₂ → CH + H reaction was employed to follow C(¹D) decays by monitoring vacuum ultra violet laser induced fluorescence of the atomic hydrogen product at 121.567 nm. The deactivation rates are seen to increase at lower temperature indicating the likely influence of the CNN intermediate complex lifetime on intersystem crossing for this system. We also performed electronic structure calculations of relevant C(³P)-N₂ and C(¹D)-N₂ potential energy curves as well as triplet-singlet spin-orbit coupling terms using the explicitly correlated internally contracted multireference configuration interaction method (*ic*-MRCI-F12). The calculations were performed for the collinear and perpendicular approach of the C atom towards the N₂ molecule which allowed us to construct the approximate spherical (isotropic) potential model of C-N₂(j=0). The computed reduced dimensional potentials were used in quantum close coupling scattering calculations of the electronic quenching cross sections and rate constants. While the calculated potential energy curves form the basis for a good qualitative description of the reaction, the calculated rate constants are significantly smaller than the measured ones, and fail to reproduce the temperature dependence of the experimental results. Several possible reasons are provided to explain the origin of these differences.

1 Introduction

As atomic carbon is an important species in combustion, hydrocarbon synthesis and in interstellar space, considerable attention has been paid to its chemistry in both its ground $C(^3P)$ and excited $C(^1D)$ states. The kinetics¹⁻³ and dynamics⁴⁻⁷ of $C(^3P)$ reactions have been well studied for a number of years by both theoretical and experimental means with a particular emphasis on those processes involving saturated and unsaturated hydrocarbon compounds. Experimental measurements of $C(^1D)$ reactions are less numerous, given the lack of convenient clean sources of this excited atomic species. Nevertheless, certain processes such as the $C(^1D) + H_2$ reaction have been well characterized due to the possibility for comparison with the results of state-to-state quantum mechanical calculations.⁸⁻¹¹ Whilst dynamical investigations for the reactions of $C(^1D)$ with CH_4 , C_2H_2 , C_2H_4 , C_3H_6 and HCl have also been reported over a range of collision energies,¹²⁻¹⁷ very few temperature dependent kinetic studies of $C(^1D)$ reactions are available in the literature. To the best of our knowledge, the only measurements of temperature dependent rate constants for $C(^1D)$ reactivity were recorded by some of the present authors in very recent investigations of the $C(^1D) + CH_3OH$ and $C(^1D) + H_2$ reactions over the 50-296 K temperature range.^{18,19} While temperature dependent studies of the deactivation of excited state atomic oxygen, $O(^1D)$, are common due to its importance in the Earth's atmosphere (including kinetic measurements of non-reactive quenching with noble gases and N_2 ; see for example, Grondin et al. 2016²⁰), only room temperature kinetic measurements of non-reactive processes involving $C(^1D)$ have been reported. In common with $O(^1D)$, quenching of $C(^1D)$ back to the ground state is expected to be more efficient with the heavier noble gases than the light ones due to more efficient non-adiabatic transitions between the singlet and triplet state through increased spin-orbit coupling.²¹ Moreover, for $O(^1D)$, the transfer efficiency is seen to be a relatively

temperature independent process.^{20,22} For both O(¹D) and C(¹D) collisions with N₂, no exothermic product channels are available, so that the only other possible outcome is quenching to the triplet ground state through intersystem crossing. Interestingly, the measured increase in the rate for non-reactive quenching of O(¹D) with N₂,^{20,23,24} is indicative of the role played by the N₂O(X¹Σ) intermediate complex as discussed by Defazio et al.,²⁵ whereby its increased lifetime at low temperature enhances the crossing probability. In order to test this hypothesis, it is interesting to perform an investigation of the analogous C(¹D) quenching process, extending the measurements to even lower temperatures to shed more light on the role of complex formation in systems of this type.

As a secondary consideration, the C(¹D) + N₂ quenching process might be important in the atmospheres of planetary bodies such as Titan, which is primarily composed of molecular nitrogen. In Titan's upper atmosphere, the photolysis of molecules such as CO and C₃ in the vacuum ultraviolet wavelength range could lead to the production of non-negligible quantities of C(¹D) atoms.^{26,27} The fate of C(¹D) produced in this way would be highly dependent on the rate of the C(¹D) + N₂ quenching process at the appropriate low temperature. If quenching were found to be inefficient, C(¹D) would have ample time to react with the other major constituents of Titan's atmosphere, CH₄¹⁶ and H₂.¹⁹ The only previous measurements of the rate constant for the C(¹D) + N₂ reaction were reported by Braun et al.²⁸ and by Husain & Kirsch²⁹ using vacuum ultraviolet flash photolysis of carbon suboxide C₃O₂ as the source of C(¹D). The decay of these atoms was subsequently followed by absorption spectroscopy at 193 nm in the presence of an excess concentration of N₂. These authors obtained room temperature deactivation rates of $2.5 \times 10^{-12} \text{ cm}^3 \text{ molecule}^{-1} \text{ s}^{-1}$ and $(4.2 \pm 1.2) \times 10^{-12} \text{ cm}^3 \text{ molecule}^{-1} \text{ s}^{-1}$ respectively.

In this paper we report an experimental and theoretical investigation of the deactivation rate of the $C(^1D) + N_2$ reaction. Kinetic measurements were performed over the temperature range 50 – 296 K, using a supersonic flow reactor coupled with pulsed laser photolysis for $C(^1D)$ production and a vacuum ultraviolet laser induced fluorescence tracer method to follow indirectly the kinetics of $C(^1D)$ loss. Sections 2 and 3 describe respectively the experimental methods used in the present work and the results obtained. Section 4 describes the theoretical approaches used to obtain the relevant potential energy surfaces that were used in quantum scattering calculations. The theoretical results are also presented in section 4 and are discussed in light of the experimental results. Our conclusions are developed in section 5.

2 Experimental Methods

The measurements described in this paper were performed using the Bordeaux continuous supersonic flow reactor. As this technique is well documented³⁰ and the details of the present apparatus have been reported elsewhere,^{31,32} only features specific to the current investigation will be presented here. Supersonic flow temperatures of 50 K, 75 K and 127 K were generated through the use of three axisymmetric Laval nozzles employing argon as the carrier gas. As the aim of the present investigation was to obtain rate constants for the $C(^1D) + N_2$ reaction, it was not possible to use our fixed density N_2 based nozzles. Room temperature experiments (296 K) were performed in the absence of a Laval nozzle with a reduced flow velocity compared to the low temperature experiments, avoiding pressure gradients within the reactor.

$C(^1D)$ atoms were produced by the 266 nm pulsed multiphoton dissociation of CBr_4 molecules which were entrained in the flow by passing a secondary argon flow over solid CBr_4 held in a separate reservoir at a known fixed pressure. As the photolysis laser was coaligned along the reactor axis, a column of carbon atoms of uniform density was created downstream of the Laval

nozzle. The concentration of CBr_4 molecules within the supersonic flow was estimated to be less than 2×10^{13} molecule cm^{-3} . The ratio of the photolysis yield of $\text{C}(^1\text{D})$ atoms with respect to $\text{C}(^3\text{P})$, $\text{C}(^1\text{D})/\text{C}(^3\text{P})$, was found to be 0.10 - 0.15 in our previous studies of $\text{C}(^1\text{D})$ and $\text{C}(^3\text{P})$ reactions under similar conditions.^{18,19,33,34} It is also possible that low concentrations of $\text{C}(^1\text{S})$ atoms could be present in the flow. Rate constants for the $\text{C}(^1\text{S}) + \text{H}_2$ and $\text{C}(^1\text{S}) + \text{N}_2$ reactions have been measured³⁵ to be $< 5 \times 10^{-12}$ cm^3 molecule $^{-1}$ s $^{-1}$ and 3.2×10^{-12} cm^3 molecule $^{-1}$ s $^{-1}$ respectively at 300K. If these values are also considered to be valid at low temperature, the production of H-atoms from the $\text{C}(^1\text{S}) + \text{H}_2$ reaction should be negligible compared to the quenching of $\text{C}(^1\text{S})$ atoms by N_2 .

The temporal evolution of $\text{C}(^1\text{D})$ atoms could not be followed directly in the present experiments. In order to circumvent this problem, a small quantity of molecular hydrogen was added to the flow, maintained at a constant value for any single series of experiments with N_2 as the excess reagent, thereby employing the pseudo-first-order approximation. Some of the $\text{C}(^1\text{D})$ atoms present in the flow reacted with H_2 , yielding CH radicals and H-atoms as products, while the large majority of $\text{C}(^1\text{D})$ atoms were quenched to the ground state through collisions with N_2 . Under these conditions, the H-atom temporal profile derives from the total loss of $\text{C}(^1\text{D})$ atoms and not only the part leading to H-atom formation. As a result, if the N_2 concentration is varied (with $[\text{H}_2]$ fixed), the change in the H-atom temporal profile is entirely due to the different $[\text{N}_2]$. The kinetics of the fitting procedure used to extract rate constants is explained in more detail in the results section. The H-atoms themselves were detected by on-resonance vacuum ultraviolet laser induced fluorescence (VUV LIF) using the $1s\ ^2\text{S} \rightarrow 2p\ ^2\text{P}^0$ Lyman- α transition at 121.567 nm. A 10 Hz Nd:YAG pumped dye laser operating at 729.4 nm was frequency doubled by a type I BBO crystal. This beam at 364.7 nm was directed and focused into a cell containing 210 Torr

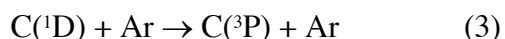
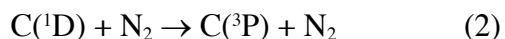
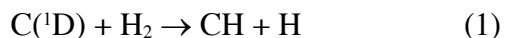
of Kr with 550 Torr of Ar for phase matching, producing the required VUV wavelength by third harmonic generation. The resulting VUV beam was collimated by a magnesium fluoride lens at the cell exit which was positioned at the reactor observation axis, perpendicular to the supersonic flow. The VUV emission from excited H-atoms in the flow were collected by a solar blind photomultiplier tube. Typically, the measurement of kinetic profiles consisted of the accumulation of signal from 30 probe laser shots at each time interval, with at least 40 time intervals being recorded for each individual H-atom formation curve. In addition, at least 10 time intervals were recorded prior to the photolysis laser, to set the pretrigger baseline value.

The gases used in the experiments (Ar 99.999%, N₂ 99.999%, H₂ 99.9999%, Kr 99.99%) were flowed from cylinders without further purification. The use of mass-flow controllers provided precise control over their concentrations within the supersonic flow. The mass-flow controllers were calibrated using the pressure rise at constant volume method for each individual gas used.

3 Experimental Results

Example temporal profiles of the VUV LIF signal obtained by detecting atomic hydrogen (produced by the C(¹D) + H₂ reaction) in the presence of different excess N₂ concentrations at 127 K are shown in Figure 1.

Under these conditions, the kinetics of hydrogen atom formation is determined by the following reactions:





where X is any other species in the supersonic flow that removes atomic hydrogen.

C(¹D) is lost through reaction with H₂ and with its precursor CBr₄, by quenching with N₂ and the carrier gas Ar and by diffusion. The H-atom product VUV LIF signal (I_{H}) is characterized by a rising part followed by a slower decay, consistent with H-atoms being formed by reaction (1) and lost through reactions (6) and (7). The temporal profiles of atomic hydrogen obtained at 127 K shown in Figure 1 were obtained in the presence of high (3.4×10^{15} molecule cm⁻³) and low (4.3×10^{14} molecule cm⁻³) N₂ concentrations.

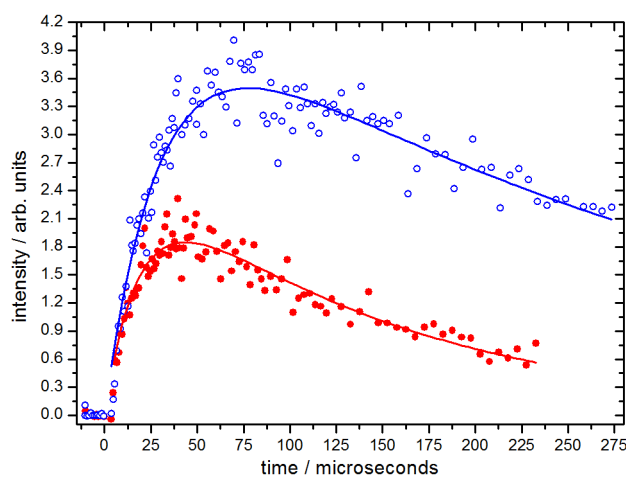


Figure 1 H-atom fluorescence signals as a function of time recorded at 127 K. (Blue open circles) $[\text{N}_2] = 4.28 \times 10^{14}$ molecule cm⁻³. (Red filled circles) $[\text{N}_2] = 3.36 \times 10^{15}$ molecule cm⁻³. The lower H-atom signal amplitude at higher $[\text{N}_2]$ results from an increased loss by quenching (see text). The fits to the data begin after a few microseconds have elapsed due to negative baseline values which arise as the photolysis laser passes close to the gate of the boxcar.

The H-atom signal is represented by the following biexponential function:

$$I_H = A\{\exp(-k'_L t) - \exp(-k'_F t)\}$$

where A is a constant representing the theoretical amplitude of the H-atom signal in the absence of competing loss processes and k'_F and k'_L are the pseudo-first-order rate constants for H-atom formation and loss respectively.

k'_F governs the rise time of the H-atom signal and comprises several terms:

$$k'_F = \sum k_{H_2}[H_2] + k_{N_2}[N_2] + k_{CBr_4}[CBr_4] + k_{Ar}[Ar] + k_{diff,C(1D)}$$

$k_{H_2}[H_2]$, $k_{Ar}[Ar]$, $k_{CBr_4}[CBr_4]$ and $k_{diff,C(1D)}$ are the pseudo-first-order rates for processes (1), (3), (4) and (5) which are constant terms as $[H_2]$, $[Ar]$ and $[CBr_4]$ are fixed for any series of measurements. $k_{N_2}[N_2]$ is the pseudo-first-order rate for reaction (2), meaning that k'_F varies as a function of $[N_2]$ for any series of measurements. Nevertheless, as the fraction of C(1D) lost through quenching increases with $[N_2]$, the H-atom signal amplitude should decrease at higher $[N_2]$. Hence the uncertainty of H-atom profiles recorded at high $[N_2]$ will be larger than the corresponding low $[N_2]$ ones.

k'_L governs the slow decay of the H-atom signal which is composed of two terms:

$$k'_L = \sum k_X[X] + k_{diff,H}$$

$k_X[X]$ and $k_{diff,H}$ are the first-order losses by reaction and by diffusion of atomic hydrogen respectively. In this instance, k'_L is dominated by diffusion.

A minimum of 36 H-atom decay profiles were recorded for at least 6 different N_2 concentrations at each temperature. Values of the pseudo-first-order H-atom formation rate, k'_F , were plotted against the corresponding N_2 concentration. Examples of such plots are shown in

Figure 2 with the second-order rate constant being derived from the slopes of fits to the data, weighted by the statistical uncertainty of the first-order rates.

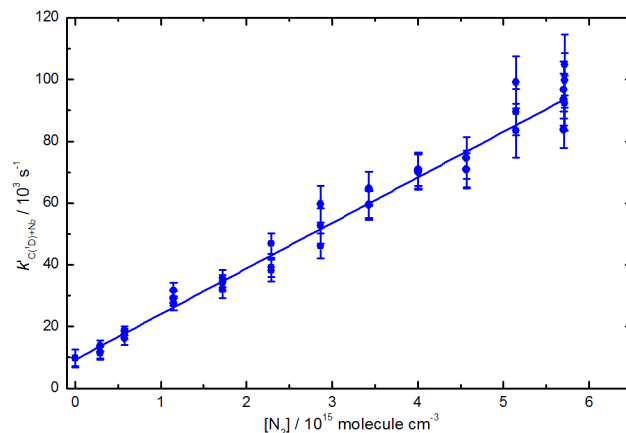


Figure 2 Pseudo-first-order rate constants for reaction (2) as a function of $[N_2]$ recorded at 50 K (blue filled circles). A weighted linear least squares fit (solid blue line) yields the second-order rate constant k_2 . The error bars reflect the statistical uncertainties at the level of a single standard deviation obtained by fitting to H-atom VUV LIF profiles such as those shown in Figure 1.

The y axis intercept value of this plot reflects the pseudo-first-order losses of $C(^1D)$ atoms by processes (1), (3), (4) and (5). In this example, $[H_2] = 1 \times 10^{13} \text{ molecule cm}^{-3}$, $[CBr_4] = 2 \times 10^{13} \text{ molecule cm}^{-3}$ and $[Ar] = 2.59 \times 10^{17} \text{ atom cm}^{-3}$. The rate constant for the $C(^1D) + H_2$ reaction has been measured at 50 K¹⁹ with a value of $2.65 \times 10^{-10} \text{ cm}^3 \text{ molecule}^{-1} \text{ s}^{-1}$ leading to a pseudo-first-order loss rate of 2700 s^{-1} . The rate constant for reaction (3) is small, with an upper limiting value of $1 \times 10^{-15} \text{ cm}^3 \text{ molecule}^{-1} \text{ s}^{-1}$ at 300 K³⁶ leading to a pseudo-first-order loss rate of 260 s^{-1} if we assume a similar rate constant at 50 K. The diffusional loss rate for $C(^1D)$ is likely to be around 3000 s^{-1} considering earlier measurements of the diffusional loss of $C(^3P)$ atoms under similar conditions.³⁴ The rate constants for reaction (4) are unknown, but it is likely these are high, with

values that might be similar to those of reaction (1). If we estimate a rate constant of 2×10^{-10} $\text{cm}^3 \text{ molecule}^{-1} \text{ s}^{-1}$ for this process, we obtain a pseudo-first-order loss rate of 4000 s^{-1} . The sum of these pseudo-first-order loss rates is thus entirely consistent with the measured ones in the absence of N_2 .

The measured rate constants are presented as a function of temperature in Figure 3 and are summarized alongside other relevant information in Table 1.

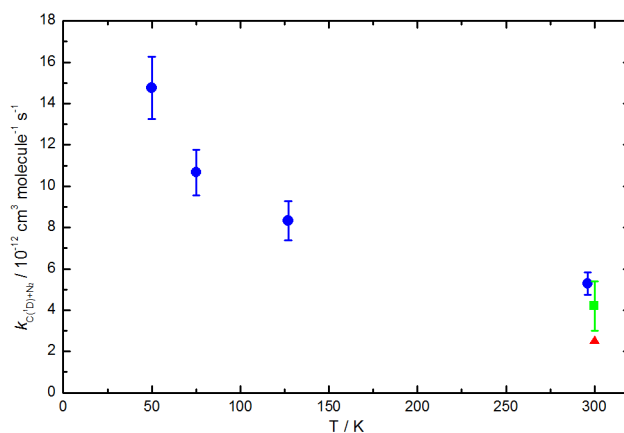


Figure 3 Rate constants for the $\text{C}(^1\text{D}) + \text{N}_2$ reaction as a function of temperature. Braun et al.²⁸ (red filled triangle); Husain & Kirsch²⁹ (green filled square); this work (blue filled circles). Experimental uncertainties represent the combined statistical errors on the second-order rates and include estimated systematic errors (10 %).

Table 1 Measured rate constants for the $\text{C}(^1\text{D}) + \text{N}_2$ reaction

| T / K | $[\text{N}_2]_{\text{max}} / 10^{15}$ molecule cm^{-3} | Flow density / 10^{16} molecule cm^{-3} | N^a | $k_2 / 10^{-12}$ $\text{cm}^3 \text{ molecule}^{-1} \text{ s}^{-1}$ |
|----------------|--|---|-------|--|
| 50 ± 1^b | 5.7 | 25.9 ± 0.9^b (Ar) | 38 | 14.8 ± 1.5^c |
| 75 ± 2 | 4.1 | 14.7 ± 0.6 (Ar) | 39 | 10.7 ± 1.1 |
| 127 ± 2 | 3.4 | 12.6 ± 0.3 (Ar) | 36 | 8.3 ± 0.9 |

| | | | | |
|-----|------|-----------|----|---------------|
| 296 | 11.3 | 16.3 (Ar) | 46 | 5.3 ± 0.5 |
|-----|------|-----------|----|---------------|

^a Number of individual measurements.

^b The errors on the temperature and flow density, cited at the level of one standard deviation are calculated from separate measurements of the impact pressure using a Pitot tube as a function of distance from the Laval nozzle and the stagnation pressure within the reservoir.

^c The uncertainties on the second-order rates were calculated from the statistical uncertainty of the pseudo-first-order rates and include systematic errors. Systematic errors could have arisen from inaccuracies in the measured flow rates, pressures and temperatures and have been estimated to have an upper limit of 10%.

The measured room temperature rate of $(5.3 \pm 0.5) \times 10^{-12} \text{ cm}^3 \text{ molecule}^{-1} \text{ s}^{-1}$ is seen to be slightly larger than the previous measurement by Braun et al.,²⁸ but it agrees well with the value obtained by Husain & Kirsch²⁹ of $(4.2 \pm 1.2) \times 10^{-12} \text{ cm}^3 \text{ molecule}^{-1} \text{ s}^{-1}$ using a different detection method. The quenching rate constants show a clear negative temperature dependence, increasing to a value of $(14.8 \pm 1.5) \times 10^{-12} \text{ cm}^3 \text{ molecule}^{-1} \text{ s}^{-1}$ at 50 K. This increase is more pronounced for the C(¹D) + N₂ reaction than the one measured for the equivalent O(¹D) + N₂ quenching process over the same temperature range,²⁰ although the experimental rate constants for the title reaction are approximately 5 times smaller.

4 Theoretical approach

In order to have an insight into the behavior of the experimental rate constants, we performed a theoretical study of the title process. The first step of a collisional study consists in the determination of the interaction potentials between colliding particles. Computing global C(³P)-N₂ and C(¹D)-N₂ potential energy surfaces and the corresponding spin-orbit couplings represents a very challenging task. Their use in exact quantum scattering calculations is even more complex. This is why we decided to use a reduced dimensional approach where the N₂ molecule is described as a structureless sphere. Such an approach implies to fix the N₂ intermolecular

distance and to compute the interaction potential for limited N_2 orientations. The scattering calculations are, in that case, equivalent to atom-atom collisions. Using such an approximate treatment, we do not expect quantitative agreement between theoretical and experimental data.

Interaction Potentials

The C- N_2 PESs are described by the two Jacobi coordinates R the distance from the center of mass of N_2 molecules to the C atom, and θ , the angle between R and the N_2 bond axis r . We consider that the N_2 molecule only approaches the carbon atom collinearly ($\theta=0^\circ$) or perpendicularly ($\theta=90^\circ$) and we describe the electronic states that arise in terms of the representations of the C_{2v} group of symmetry. The approach of the N_2 molecule will lift the 3-fold degeneracy of the ground electronic $C(^3P)$ term causing the appearance, in the collinear geometry, of two triplet states, the ground $X^3\Sigma^-$ and doubly-degenerate $A^3\Pi$. In the case of the excited term $C(^1D)$ lying 10000 cm^{-1} above the ground state of the C atom, the five-fold degeneracy is lifted by the N_2 forming first the lower lying doubly-degenerate $a^1\Delta$ state, then the $b^1\Sigma^+$ state and finally the doubly-degenerate $1^1\Pi$ state.

We use the explicitly correlated version³⁷ of the internally contracted multi-reference configuration interaction method³⁸ with single and double excitation and Davidson correction³⁹ for higher excitations (Q), ic-MRCISD-F12+Q, for calculations of the potential energy curves originating from the interaction of the C atom in its 3P and 1D electronic terms with the ground electronic state of the N_2 molecule. We employ the augmented, correlation-consistent triple-zeta basis set with density fitting basis (JKFIT/MP2FIT) as implemented in the MOLPRO program.^{40,41} This basis together with tailored density fitting basis for the explicitly correlated method provides almost complete basis set quality results with great computational savings. The reference wave functions were obtained from state-averaged complete active space self-

consistent field (SA-CASSCF) calculations with 14 electrons distributed among 12 orbitals in the active space spanned by $2s$ and $2p$ valence orbitals of C and N atoms. The remaining six electrons were distributed among three core orbitals ($1s$), which were kept frozen in the MRCI-F12 calculations. The state averaging was done for three triplet and five singlet states. The interaction energy was calculated with respect to the asymptotic energy at $R = 200$ bohr and was not corrected for the basis set superposition error. We have also computed spin-orbit (SO) transition matrix elements⁴² between singlet and triplet states of C-N₂ under consideration using MRCISD-F12 electron densities and Breit-Pauli Hamiltonian. All the calculations have been performed with the MOLPRO 2012 suite of *ab initio* codes.⁴¹

A. Collinear Potential Curves ($\theta=0^\circ$)

The potential energy curves for the collinear approach of the N₂ molecule towards the C atom are shown in Figure 4. The $^3\Sigma^-$ and $^3\Pi$ electronic states shown correlate to the C(3P)-N₂($X^1\Sigma_g^+$) asymptotic limit and the $^1\Delta$, $^1\Sigma^+$ and $^1\Pi$ electronic states correlate to the excited state C(1D)-N₂($X^1\Sigma_g^+$) asymptote. The formation of the ground state CNN($X^3\Sigma^-$) radical is exothermic with the MRCISD-F12 exothermicity calculated to be 11368.98 cm⁻¹ (-32.5 kcal/mol). Clifford et al.⁴³ estimated the endothermic dissociation of the CNN(X) to C(3P) + N₂ products to be 37 ± 3 kcal/mol, which is in fairly good agreement with our calculated value. The $X^3\Sigma^-$ curve exhibits a small submerged (below the asymptotic threshold) barrier of 253.14 cm⁻¹ before the deep minimum of the CNN(X) radical. This barrier is located at a distance of $R = 4.85$ bohr. As a result, the C(3P) + N₂ \rightarrow CNN($X^3\Sigma^-$) association reaction is also barrierless although in this case there are no possible bimolecular product channels. The van der Waals minimum of the $X^3\Sigma^-$ state is 487.4 cm⁻¹ deep located at $R = 5.9$ bohr. The formation of the excited state $a^1\Delta$ seems to evolve on the $^1\Delta$ curve without a barrier. There are higher lying electronic terms of the collinear

CNN radical, $b^1\Sigma^+$, $A^3\Pi$ and $1^1\Pi$ with fairly deep minima for which we show interatomic distances and excitation energy data in Table 2. The excitation energies compared to previous theoretical results of Pd et al.⁴⁴ and the experiment of Clifford et al.⁴³ are in very good agreement. The theoretical values were corrected from zero point energy (ZPE) using the following method: We have optimized the $C(^3P)+N_2$ channel to get the N_2 ZPE and optimized the CNN and NCN molecules at the MRCIF12/AVTZ level. Both CNN and NCN are collinear. The difference in ZPE compared to the asymptote is 255 cm^{-1} . The geometry optimization with MRCIF12/AVTZ for collinear CNN leads to the following parameters: $R_{CN} = 1.236\text{ \AA}$ and $R_{NN} = 1.198\text{ \AA}$. There is another isomer corresponding to the $NCN(^3\Sigma)$ collinear arrangement. This molecule is energetically stable and lying 22813 cm^{-1} below the $C(^3P)-N_2$ channel and is a global minimum of the CN_2 system. The optimized RCN bond length in NCN is 1.228 \AA . The barriers on the triplet surfaces for collinear and perpendicular approach of C to N_2 are sufficiently large enough to close that channel. There is a smaller barrier of around 1093 cm^{-1} at perpendicular approach with respect to $C(^1D)-N_2$ channel to form a singlet excited state of bent CN_2 belonging to the C_{2v} symmetry group. Another product channel to consider is $CN(^2\Pi)+N(^4S)$, but this channel is 20204 cm^{-1} (without ZPE correction) above the $C(^3P)-N_2$ asymptotic channel and is well above the $C(^1D)-N_2$ channel and therefore inaccessible under the present experimental conditions.

The approach of the N_2 molecule to the $C(^1D)$ carbon atom will evolve on the $^1\Delta$ state for relatively low collision energies and will experience crossing at $R \approx 5$ bohr (therefore slightly before the submerged barrier on the $X^3\Sigma^-$ state) with the $^3\Pi$ adiabatic curve correlating to the ground state $C(^3P)-N_2$ products.

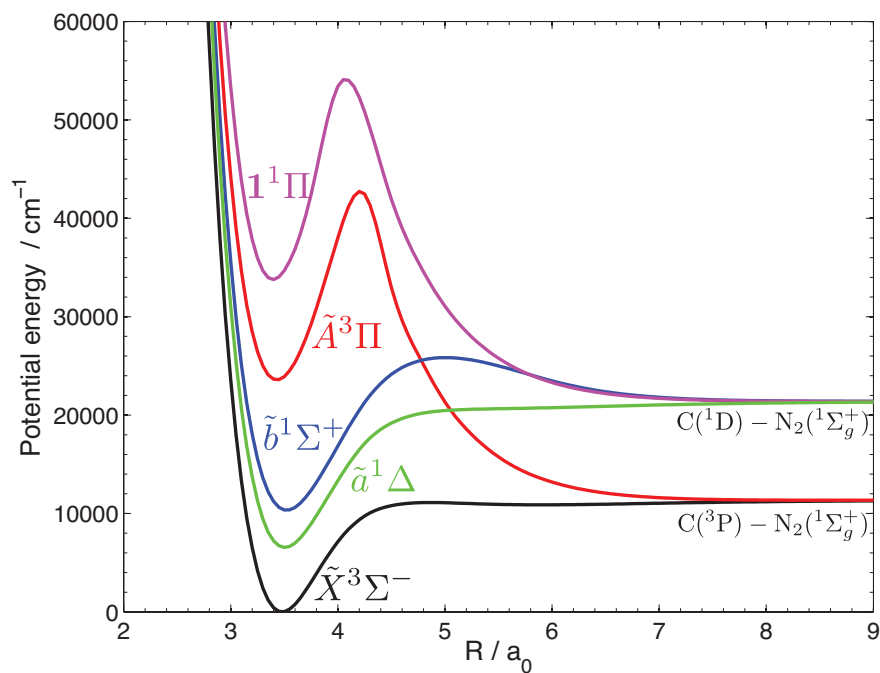


Figure 4 Potential energy curves for the collinear approach ($\theta = 0^\circ$) of the C atom to the N_2 molecule correlating with the ground $C(^3P)$ - N_2 and excited $C(^1D)$ - N_2 asymptote. For each Jacobi distance R the $r(N-N)$ distance is optimized for the $^1\Delta$ state at the CASSCF/AVTZ level.

Table 2 Equilibrium geometries and adiabatic excitation energies (this work, without zero-point energy) for the ground and first few excited electronic states of the linear CNN radical.

| State | Interatomic Distances ^a / Å | | Interaction Energies ^a / cm ⁻¹ | | |
|-----------------------|--|----------|--|------------------------|-------------------|
| | $r(C-N)$ | $r(N-N)$ | MRCI-F12 | Pd et al. ^b | Experiment |
| $1^1\Pi$ | 1.2095 | 1.1741 | 34023 | 33010 | ... |
| $\tilde{A}^3\Pi$ | 1.2259 | 1.1784 | 23825 | 23850 | 23850 ± 120^d |
| $\tilde{b}^1\Sigma^+$ | 1.2711 | 1.1864 | 10588 | 12115 | 10690 ± 120^c |
| $\tilde{a}^1\Delta$ | 1.2616 | 1.1852 | 6803 | 7879 | 6830 ± 120^c |
| $\tilde{X}^3\Sigma^-$ | 1.2494 | 1.1833 | 0 | 0 | 0 |

^aValues correspond to the minima shown in Figure 4. The $r(\text{N-N})$ distance corresponds to the value optimized for the $^1\Delta$ state at the CASSCF level at each Jacobi distance R . It is not the true equilibrium distance for each of the particular states.

^bPd et al.⁴⁴

^cClifford et al.⁴³

^dTentative assignment

B. Perpendicular Potential Curves ($\theta=90^\circ$)

The potential energy curves for the perpendicular approach of the C atom towards the N_2 molecule are shown in Figure 5. The two Π and two Δ triplet and singlet states that were degenerate in the collinear approach will split in this case into B_1 and B_2 and A_1 and A_2 representations of the C_{2v} symmetry group, respectively. Therefore we label the states with the representations of the C_{2v} group and the 3A_2 term will correspond to the $^3\Sigma^-$ state, 3B_1 to $^3\Pi_x$, 3B_2 to $^3\Pi_y$ (and similarly for singlet states), 1A_1 will contain $^1\Sigma$ and $^1\Delta_{x^2-y^2}$ states and 1A_2 will correspond to the $^1\Delta_{xy}$ state. The lowest state with a deep minimum at short distance is the 1A_1 state, which is $^1\Delta_{x^2-y^2}$. The other states have usually long range minima and are repulsive, with some minima formed at short distances, for example in the 3B_1 or 1B_1 cases.

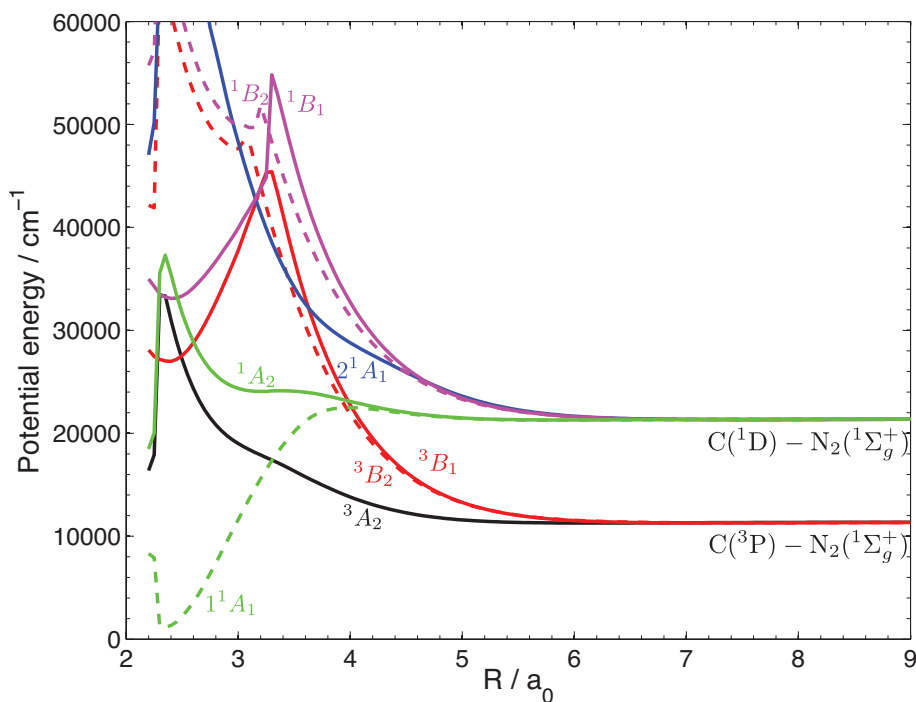


Figure 5 Potential energy curves for the perpendicular ($\theta = 90^\circ$) approach of the C atom to the N_2 molecule correlating with the ground $\text{C}(^3\text{P})\text{-N}_2$ and excited $\text{C}(^1\text{D})\text{-N}_2$ asymptote. For each Jacobi distance R the $r(\text{N-N})$ distance is optimized for the $^1\text{A}_1(^1\Delta)$ state at the CASSCF/AVTZ level. The interaction energies are expressed with respect to the $\text{X}^3\Sigma^-$ collinear minimum.

In Figure 6 we show how the interatomic distance of the N_2 molecule changes during the collinear and perpendicular approaches (the insert shows the atomic arrangements for these two approaches) optimized at the CASSCF level for the $^1\Delta$ state. One can see that the N_2 molecule stretches by about 0.2 bohr in comparison to the asymptotic equilibrium value upon the formation of the collinear CNN radical. For the perpendicular approach the N_2 molecule is enlarged by the approaching C atom to form a bent CN_2 radical. Such plots clearly show that the rigid N_2 approach is approximate and could be responsible for significant uncertainties in the rate constant calculations.

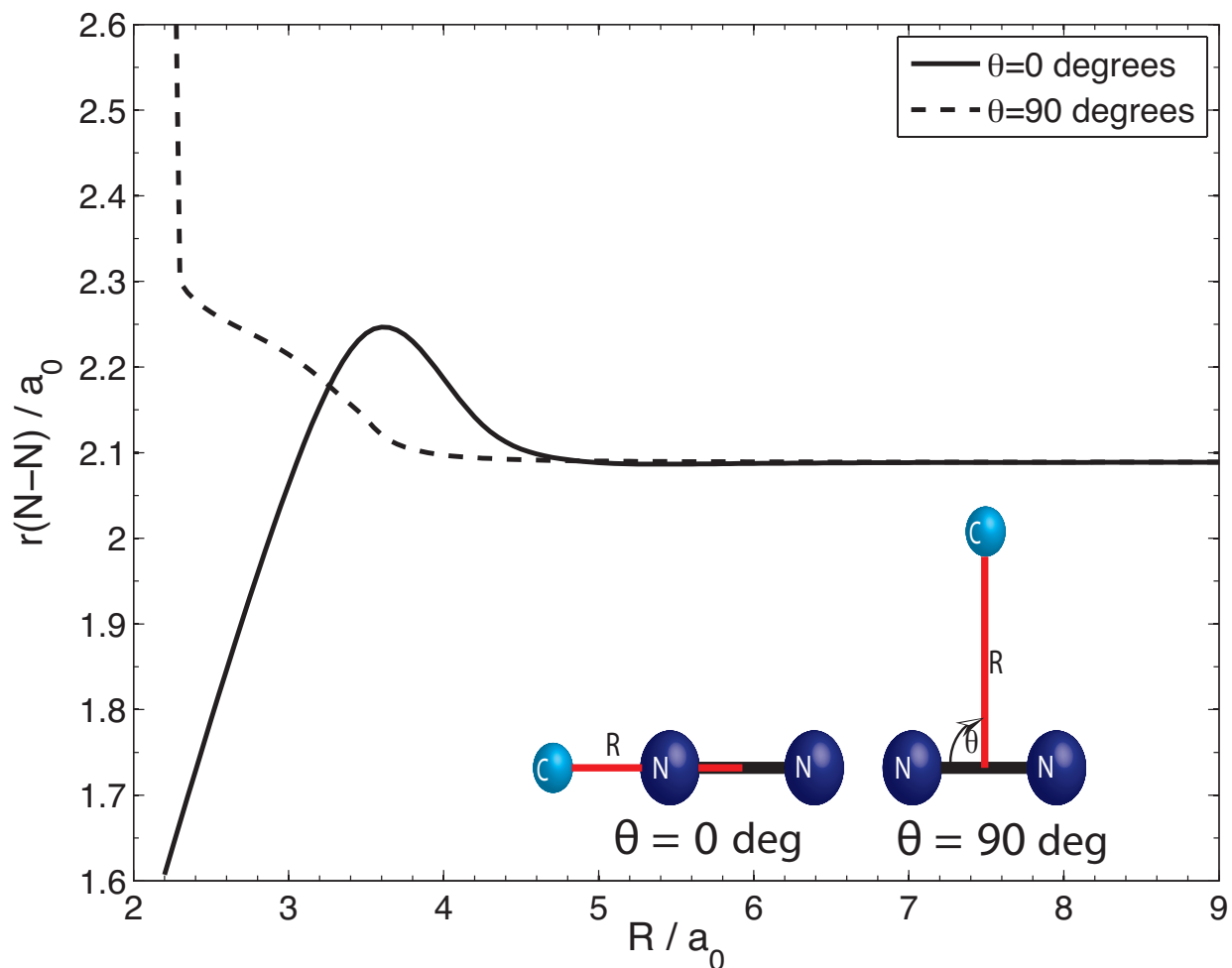


Figure 6 Plot of the optimized diatomic $r(\text{N} - \text{N})$ distance at the CASSCF/AVTZ level for the collinear ($\theta = 0^\circ$) and perpendicular ($\theta = 90^\circ$) C-N₂ approaches at each distance R for the $^1\Delta$ state.

C. Spherically averaged potentials

To obtain the potentials for the approach of the C atom to the spherical N₂, we averaged the above potentials obtained for $\theta = 0^\circ$ and $\theta = 90^\circ$ degrees by using the following formula:

$$V_{av}^i(R) = \frac{1}{5} [2V^i(R, \theta = 0^\circ) + 3V^i(R, \theta = 90^\circ)]$$

where i denotes $^3\Sigma^-$, $^3\Pi_x$, $^3\Pi_y$ for the triplets and $^1\Sigma^+$, $^1\Pi_x$, $^1\Pi_y$, $^1\Delta_{xy}$ and $^1\Delta_{x^2-y^2}$. As described above, the P and D electronic states are not degenerate in the perpendicular potential curves. This is why two sets of average potentials were obtained. We show these averaged potential curves in Figure 7. There is a van der Waals local minimum of -247 cm^{-1} with respect to the non-relativistic $C(^3P)\text{-N}_2$ asymptotic limit on the lowest $X^3\Sigma^-$ potential located at $R = 6.0$ bohr. On the same average potential there is a barrier of 337 cm^{-1} above the $C(^3P)\text{-N}_2$ asymptotic limit. The global minimum on the average $^3\Sigma^-$ potential is located at $R_e = 3.55$ bohr and is 1630 cm^{-1} deep. The $^3\Pi_x$ average potential has a shallow van der Waals minimum of 40 cm^{-1} at $R_e = 8.1$ bohr. The $^3\Pi_y$ potential has a similarly shallow minimum of 34 cm^{-1} at $R_e = 8.2$ bohr. In general, the $^3\Pi_x$ and $^3\Pi_y$ average potentials are very similar to each other and can be treated as being approximately degenerate up to a distance of 4.5 bohr. There are two interesting intersystem crossings from the point of view of energetic accessibility in the quenching process. The first one is between the $^1\Delta$ and $^3\Pi$ potentials located at $R = 4.61$ bohr with an energy of 9600 cm^{-1} above the $C(^3P)\text{-N}_2$ asymptote, but around 435 cm^{-1} below the excited state $C(^1D)\text{-N}_2$ asymptotic limit. The second one is located at shorter distance between the $^1\Delta_{x^2-y^2}$ state that is characterized by the deep minimum with respect to the $C(^1D)\text{-N}_2$ asymptotic limit. This crossing is at $R = 3.09$ bohr at an energy of 5230 cm^{-1} above the $C(^3P)\text{-N}_2$ asymptote and 4196 cm^{-1} below the $C(^1D)\text{-N}_2$ asymptotic limit. Both $^1\Delta$ states can also be treated as being approximately degenerate up to a distance of 4.5 bohr. There is another intersystem crossing accessible only for higher collision energies of $C(^1D)$ atoms. This crossing is between the $^1\Sigma$ and $^3\Pi$ curves at $R = 4.4$ bohr and at an energy of 13790 cm^{-1} above the $C(^3P)\text{-N}_2$ asymptote, which is approximately 3760 cm^{-1} above the $C(^1D)\text{-N}_2$ asymptotic limit. Therefore, collision energies of $C(^1D)$ with N_2 of around 4000 cm^{-1} are needed to access this crossing. The remaining singlet $^1\Sigma$ and $^1\Pi$ curves are mostly repulsive,

save for shallow minima at long range. The $^1\Sigma$ curve exhibits a local minimum at shorter distance, similar to the $^3\Pi$ curves, originating from the electronic states of the linear CNN radical.

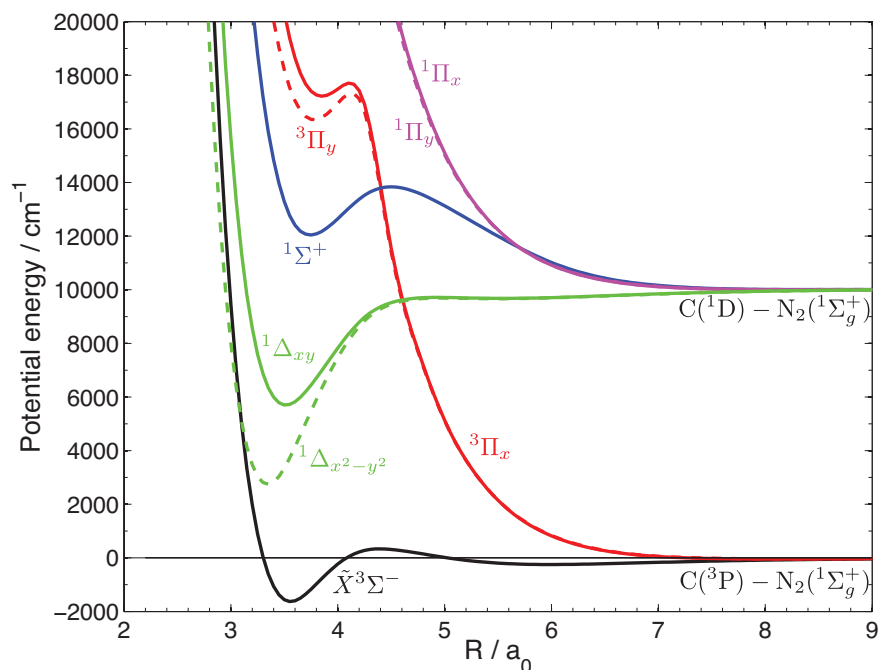


Figure 7 Spherically averaged potential energy curves for the C-N₂(j = 0) system correlating with the ground C(³P)-N₂ and excited C(¹D)-N₂ asymptote.

D. Spin-Orbit Coupling Matrix Elements

The calculated spherically averaged Spin-Orbit (SO) matrix elements that are employed in the scattering calculations are shown in Figures 8 and 9 for the elements between the Cartesian triplet projection state and between singlet and triplet projection states, respectively. Up to a distance of $R = 4$ bohr the geometry dependence of the SO matrix elements is quite negligible, at short distances, where the linear CNN radical is formed, the SO matrix elements change more rapidly, but these are still within ten or a couple of tens of cm^{-1} , which is much less in

comparison to the interaction energy in this region. Generally, the values of the SO matrix elements are fairly small, similar to the perpendicular approach. After spherical averaging, their values are in the range $-20 - +20 \text{ cm}^{-1}$. The variation of the SO matrix elements is much less pronounced than in for example the Xe-O(^1D)/(^3P) quenching system.⁴⁵ This will directly affect the degree of the quenching process. We refer the reader to work of Dagdigian et al.⁴⁵ for the details of how the SO matrix elements are introduced in the scattering Hamiltonian.

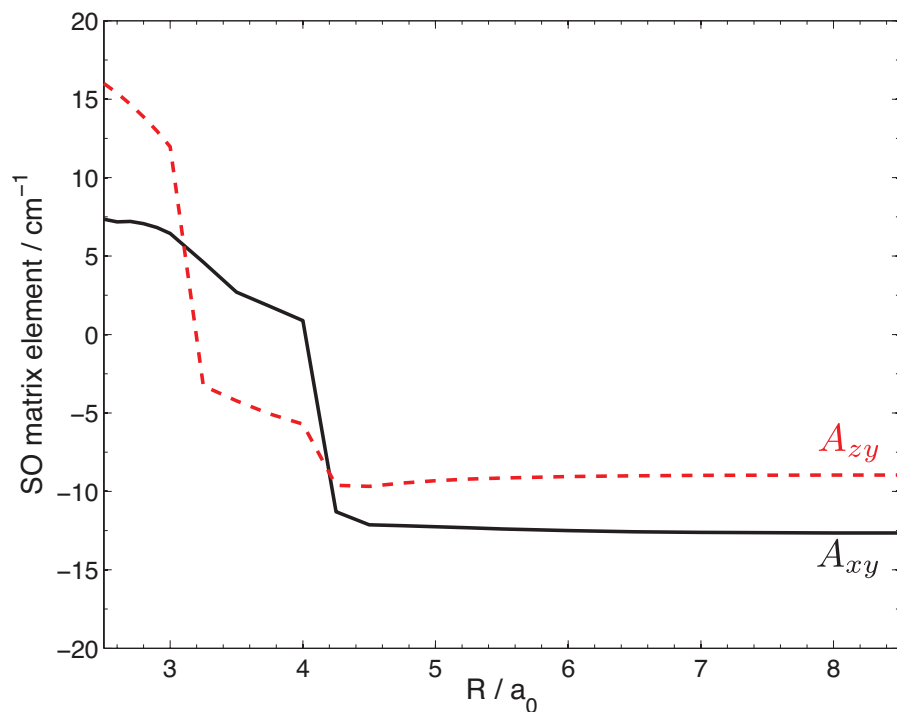


Figure 8 Spherically averaged Spin-Orbit (SO) matrix elements between the projection states of the C(^3P)-N₂ Cartesian triplet wave functions calculated at the MRCISD-F12 level of theory: $A_{xy} = \langle 1^3\Pi_x | \hat{L}_z \hat{S}_z | 1^3\Pi_y \rangle$, $A_{zy} = \langle 1^3\Pi_x | \hat{L}_x \hat{S}_x | 1^3\Sigma \rangle$.

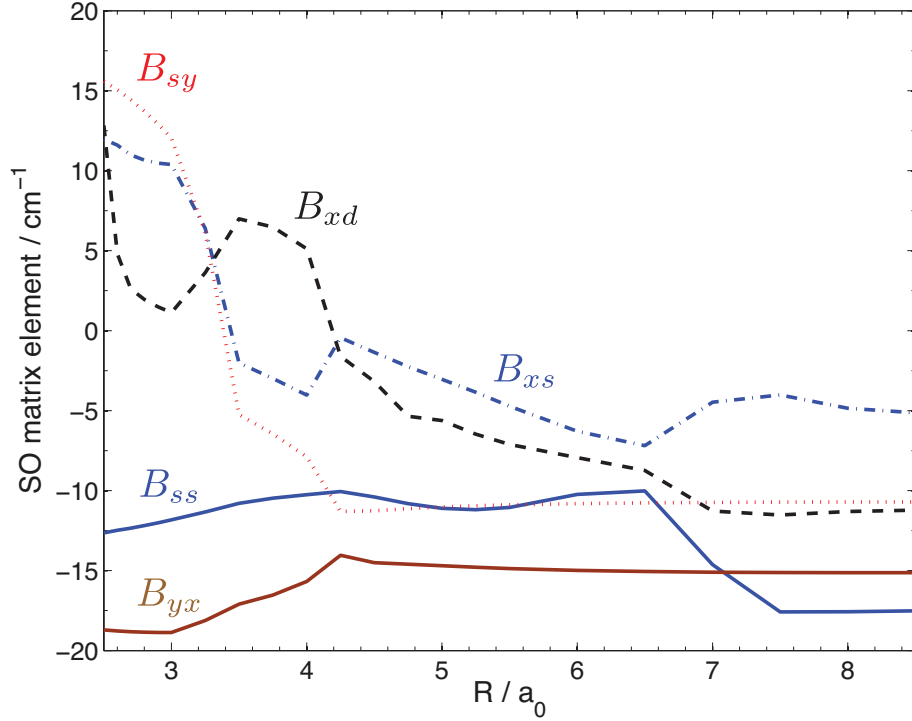


Figure 9 Spherically averaged Spin-Orbit (SO) matrix elements between the projection states of the $C(^3P)\text{-N}_2$ Cartesian triplet and $C(^1D)\text{-N}_2$ singlet wave functions calculated at the MRCISD-F12 level of theory: $B_{sy} = \langle 1^3\Sigma | \hat{L}_y \hat{S}_y | 1^1\Pi_y \rangle$, $B_{xd} = \langle 1^3\Pi_x | \hat{L}_x \hat{S}_x | 1^1\Delta \rangle$, $B_{xs} = \langle 1^3\Pi_x | \hat{L}_y \hat{S}_y | 1^1\Sigma \rangle$, $B_{ss} = \langle 1^3\Sigma | \hat{L}_z \hat{S}_z | 1^1\Sigma \rangle$, $B_{yx} = \langle 1^3\Pi_y | \hat{L}_z \hat{S}_z | 1^1\Pi_x \rangle$.

Quantum Scattering calculations

As discussed above, we have restricted the scattering problem to atom-atom collisions. In order to compute the inelastic cross sections and the corresponding rate coefficients, we use the formalism described in Dagdigian et al.⁴⁵

In atom-atom collisions, the P and D electronic states are degenerate. As seen above, the P and D electronic states are no longer degenerate in the spherically averaged potential. Whereas the P states are almost degenerate and can be considered as such in the scattering calculations, the two D states significantly differ. Then, we decided to perform two sets of calculations considering

both ${}^1\Delta_{xy}$ and ${}^1\Delta_{x^2-y^2}$ as the ${}^1\Delta$ electronic state. Time-independent quantum scattering calculations were carried out with the HIBRIDON suite of programs.⁴⁶ Convergence of the cross sections was checked with respect to the sector width in the radial integration and the number of partial waves. The calculations included all partial waves with total angular momenta $J \leq 130$. We have also performed calculations for the cut of the potential and SO coupling matrix elements corresponding to the collinear arrangements of C and N₂, for $\theta = 0^\circ$. This way we can probe how the scattering results are sensitive to the potential averaging.

Cross sections were calculated on a grid of 5099 total energies over the range $10218 \leq E_{\text{tot}} \leq 14218 \text{ cm}^{-1}$. From the inelastic cross sections $\sigma(E_C)$, one can obtain the corresponding thermal rate coefficients at temperature T by an averaging over the collision energy (E_C):

$$k_{i \rightarrow j}(T) = \left(\frac{8}{\pi \mu k^3 T^3} \right)^{1/2} \int_0^\infty \sigma_{i \rightarrow j}(E) E \exp(-E/kT) dE$$

where k_B is the Boltzmann constant, and i and f denote the initial and final levels of the colliders, respectively. Calculations of the cross sections at total energies up to 3000 cm^{-1} allow the determination of rates up to 300 K without loss of accuracy.

In Figures 10 and 11, we show the calculated total quenching cross sections and rate constants, respectively, with spherically averaged potentials and with the potentials for the collinear approach. Both spherical potentials with different Δ potentials give very similar cross sections and rates while the potential for the collinear approach results in increased cross sections and rate constants. The total quenching rate constants obtained using spherically averaged potentials are 2 orders of magnitude smaller than corresponding experimental results. While the general trend of the temperature dependence is qualitatively similar, the experimental quenching rate constant increases much faster than the calculated one with decreasing temperature. The rate constants

obtained with the collinear potential do not reproduce the experimental temperature dependence of the quenching process either. This clearly indicates that there are some anisotropic effects in the C + N₂ quenching collisions.

The major differences between the theoretical and experimental data can certainly be explained by the crude approximations that have been used in the theoretical calculations. Indeed, we considered N₂ as a rigid rotor, we neglected the rotation of the N₂ molecules and the non-adiabatic couplings were ignored. All these approximations lead to significant underestimations of the rate constants. In particular, the large difference between the spherically averaged and collinear approach emphasizes the importance of the rotation of the N₂ molecules for a correct description of the process. Such conclusions could have been anticipated on the basis of previous studies that have already shown that neglecting the rotation of the projectile could result in a significant underestimation of the collisional rate coefficients.⁴⁷ It is however difficult to estimate the real impact of the other approximations even if we can also anticipate that neglecting the non-adiabatic coupling will also lead to an underestimation of the quenching rates. From a classical point of view, in the case of atom-atom collisions (the formalism used here) the system passes through the crossing point of the singlet-triplet states only twice. One time from the entrance valley toward bond formation, and the second time towards separation of the two atoms. The temperature dependence of the quenching rate is then governed mostly by long range interactions, leading to a relatively weak effect.^{22,45,48} In the case of atom + molecule reactions, the system will explore a much more complex potential surface due to the extra degrees of freedom neglected here. As the lifetime of the CNN intermediate will increase with decreasing temperature (leading to a notable increase of the number of passages through the crossing point), the quenching rate is also expected to increase at lower temperature.

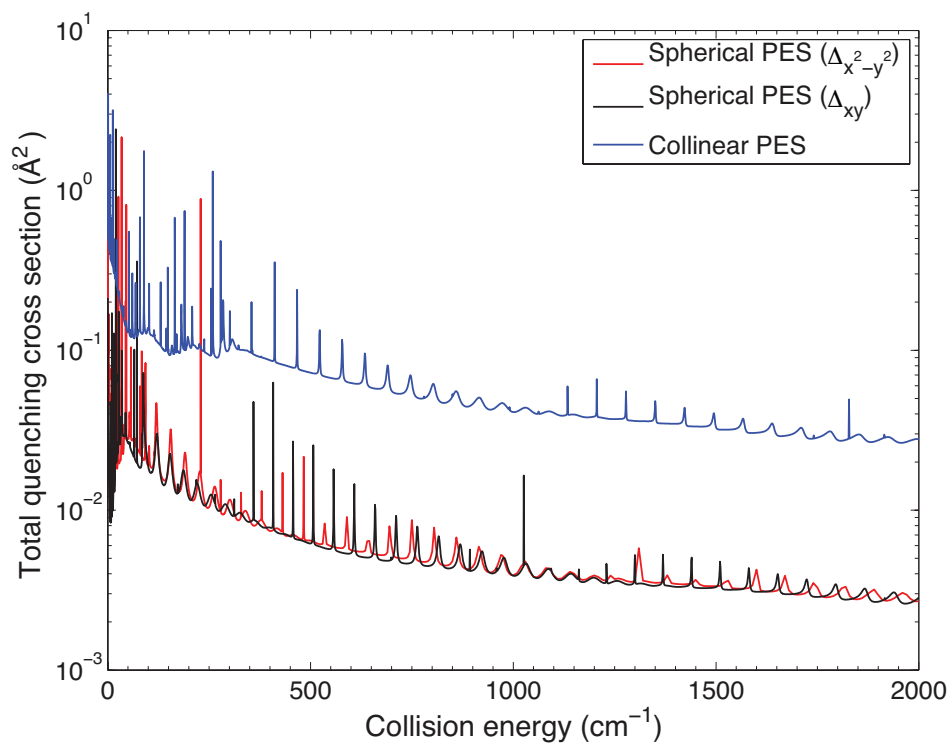


Figure 10 Total quenching cross sections from the initial C(¹D)-N₂ to all final C(³P)-N₂ states from the scattering calculations with spherical potentials with the ¹Δ_{xy} (solid black line) or ¹Δ_{x²-y²} (solid red line) state used as the ¹Δ state and with the collinear PES (dashed blue line).

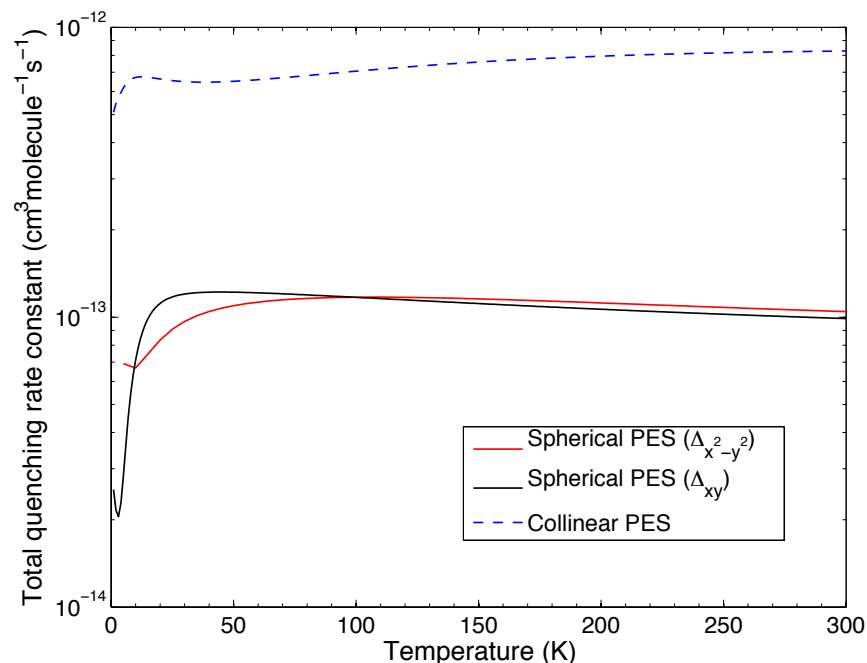


Figure 11 Total quenching rate constants from the initial C(¹D)-N₂ to all final C(³P)-N₂ states from the scattering calculations with spherical potentials with the ¹Δ_{xy} (solid black line) or ¹Δ_{x²-y²} (solid red line) state used as the ¹Δ state and with the collinear PES (dashed blue line).

5 Conclusions

This paper reports an experimental and theoretical investigation of the C(¹D) + N₂ quenching reaction. Experiments were conducted over the 50 - 296 K temperature range using a continuous supersonic flow reactor, extending the available kinetic data for this processes below room temperature for the first time. C(¹D) was produced by pulsed laser photolysis of precursor CBr₄ molecules and the quenching process was followed indirectly using a tracer method whereupon H-atoms produced by the C(¹D) + H₂ reaction were followed as a function of time through vacuum ultra violet laser induced fluorescence detection. In parallel, to elucidate the pertinent reaction pathways, ab initio calculations were performed of the global potential energy surfaces

leading from $C(^1D) + N_2$ reactants and $C(^3P) + N_2$ products, including the corresponding spin-orbit couplings, using a reduced dimensionality approach. Whilst this method provided a good qualitative description of the quenching process, scattering calculations performed using these surfaces could neither reproduce the magnitude nor the temperature dependence of the experimental rate constants which were seen to increase with decreasing temperature. This disagreement is likely to originate from the various approximations used in the ab initio calculations. The increase in the experimental rate can be explained by the formation of an energized CNN intermediate species whose lifetime increases as the temperature falls, thereby enhancing the probability for non-adiabatic transitions to occur through spin-orbit coupling.

In order to evaluate the potential importance of $C(^1D)$ chemistry to planetary atmospheres such as that of Titan, we should compare its potential non-reactive losses which occur mainly through quenching with N_2 to its potential reactive losses, primarily with the other major atmospheric constituents, CH_4 and H_2 which make up approximately 5% and 0.5% of the total (mostly N_2) density respectively. If we consider 150 K as being a representative temperature for Titan's atmosphere, the rate constant for non-reactive quenching by N_2 is approximately $8 \times 10^{-12} \text{ cm}^3 \text{ molecule}^{-1} \text{ s}^{-1}$ whereas the rate constant for reaction with H_2 at 150 K¹⁹ is approximately $3 \times 10^{-10} \text{ cm}^3 \text{ molecule}^{-1} \text{ s}^{-1}$ while the rate constant of the $C(^1D) + CH_4$ reaction has never been measured. The H_2 mole fraction is roughly 200 times less than that of N_2 , while the rate constant for the H_2 reaction with $C(^1D)$ is only 40 times larger than the quenching rate, meaning that $C(^1D)$ loss is dominated by quenching. However, if we assume a rate for the $C(^1D) + CH_4$ reaction similar to the $C(^1D) + H_2$ one, reactive loss is almost a factor of two larger than non-reactive loss in this case, indicating that the $C(^1D) + CH_4$ reaction might represent an important loss process for $C(^1D)$ in Titan's atmosphere. In terms of its potential products, Leonori et al.¹⁶ performed an

experimental investigation of the branching channels for the $C(^1D) + CH_4$ reaction, using the crossed molecular beam method. They determined that the reaction proceeds by an addition-elimination mechanism leading to the formation of $H_2CC/C_2H_2 + H_2$ and $C_2H_3 + H$ as products with an equal importance for H-displacement and H_2 elimination channels. Given its potential importance as highlighted above, there is clearly a need for more precise data on the kinetics of the $C(^1D) + CH_4$ reaction over a range of temperatures.

AUTHOR INFORMATION

Corresponding Author

* Correspondence to: km.hickson@ism.u-bordeaux1.fr. Tel: +33 (0)5 40 00 63 42

* Second corresponding author: jklos@umd.edu

Author Contributions

The manuscript was written through contributions of all authors. All authors have given approval to the final version of the manuscript.

ACKNOWLEDGMENTS

We thank Prof. Paul Dagdigian for his help with the adaptation of the Hibridon scattering basis for this system. KMH, JCL and FL acknowledge support from the INSU-CNRS national programs PCMI and PNP.

REFERENCES

1 Clary, D.C.; Haider, N.; Husain, D.; Kabir, M. Interstellar Carbon Chemistry: Reaction Rates of Neutral Atomic Carbon with Organic Molecules. *Astrophys. J.* **1994**, *422*, 416-422.

2 Chastaing, D.; James, P.L.; Sims, I.R.; Smith, I.W.M. Neutral-Neutral Reactions at the Temperatures of Interstellar Clouds: Rate Coefficients for Reactions of Atomic Carbon, C(³P), with O₂, C₂H₂, C₂H₄ and C₃H₆ Down to 15 K. *Phys. Chem. Chem. Phys.* **1999**, *1*, 2247-2256.

3 Chastaing, D.; Le Picard, S.D.; Sims, I.R.; Smith, I.W.M.; Geppert, W.D.; Naulin, C.; Costes, M. Rate Coefficients and Cross-Sections for the Reactions of C Atoms with Methylacetylene and Allene. *Chem. Phys. Lett.* **2000**, *331*, 170-176.

4 Clary, D.C.; Buonomo, E.; Sims, I.R.; Smith, I.W.M.; Geppert, W.D.; Naulin, C.; Costes, M.; Cartechini, L.; Casavecchia, P. C + C₂H₂: A Key Reaction in Interstellar Chemistry. *J. Phys. Chem. A* **2002**, *106*, 5541-5552.

5 Kaiser, R.I.; Ochsenfeld, C.; Head-Gordon, M.; Lee, Y.T.; Suits, A.G. Crossed-Beam Reaction of Carbon Atoms with Hydrocarbon Molecules. III. Chemical Dynamics of Propynylidyne (l-C₃H; X²II_j) and Cyclopropynylidyne (c-C₃H; X²B₂) Formation from Reaction of C(³P_j) with Acetylene, C₂H₂(X¹Σ_g⁺). *J. Chem. Phys.* **1997**, *106*, 1729-1741.

6 Costes, M.; Halvick, P.; Hickson, K. M.; Daugey, N.; Naulin, C. Non-Threshold, Threshold, and Nonadiabatic Behaviour of the Key Interstellar C + C₂H₂ Reaction. *Astrophys. J.* **2009**, *703*, 1179-1187.

7 Naulin, C.; Daugey, N.; Hickson, K. M.; Costes, M. Dynamics of the Reactions of C-Atoms with Ethylene, Allene, and Methylacetylene at Low Energy Revealed by Doppler-Fizeau Spectroscopy. *J. Phys. Chem. A* **2009**, *113*, 14447-14457.

8 Lin, S. Y.; Guo, H. Quantum Wave Packet Studies of the C(¹D) + H₂ → CH + H Reaction: Integral Cross Section and Rate Constant. *J. Phys. Chem. A* **2004**, *108*, 2141-2148.

- 9 Defazio, P.; Petrongolo, C.; Bussery-Honvault, B.; Honvault, P. Born–Oppenheimer Quantum Dynamics of the $C(^1D) + H_2$ Reaction on the $CH_2 \tilde{a} \ ^1A_1$ and $\tilde{b} \ ^1B_1$ Surfaces. *J. Chem. Phys.* **2009**, *131*, 114303.
- 10 Defazio, P.; Bussery-Honvault, B.; Honvault, P.; Petrongolo, C. Nonadiabatic Quantum Dynamics of $C(^1D) + H_2 \rightarrow CH + H$: Coupled-Channel Calculations Including Renner-Teller and Coriolis Terms. *J. Chem. Phys.* **2011**, *135*, 114308.
- 11 Suleimanov, Y. V.; Kong, W. J.; Guo, H.; Green, W. H. Ring-Polymer Molecular Dynamics: Rate Coefficient Calculations for Energetically Symmetric (Near Thermoneutral) Insertion Reactions ($X + H_2$) \rightarrow $HX + H$ ($X = C(^1D), S(^1D)$) *J. Chem. Phys.* **2014**, *141*, 244103.
- 12 Kaiser, R. I.; Mebel, A. M.; Lee, Y. T. Chemical Dynamics of Cyclopropynylidyne ($c\text{-}C_3H; X^2B_2$) Formation from the Reaction of $C(^1D)$ with Acetylene, $C_2H_2 (X^1\Sigma_g^+)$. *J. Chem. Phys.* **2001**, *114*, 231-239.
- 13 Kaiser, R. I.; Nguyen, T. L.; Mebel, A. M.; Lee, Y. T. Stripping Dynamics in the Reactions of Electronically Excited Carbon Atoms, $C(^1D)$, with Ethylene and Propylene—Production of Propargyl and Methylpropargyl Radicals. *J. Chem. Phys.* **2002**, *116*, 1318-1324.
- 14 Costes, M.; Daugey, N.; Naulin, C.; Bergeat, A.; Leonori, F.; Segoloni, E.; Petrucci, R.; Balucani, N.; Casavecchia, P. Crossed-Beam Studies on the Dynamics of the $C + C_2H_2$ Interstellar Reaction Leading to Linear and Cyclic $C_3H + H$ and $C_3 + H_2$. *Faraday Discuss.* **2006**, *133*, 157-176.

- 15 Leonori, F.; Petrucci, R.; Segoloni, E.; Bergeat, A.; Hickson, K. M.; Balucani, N.; Casavecchia, P. Unraveling the Dynamics of the $C(^3P,^1D) + C_2H_2$ Reactions by the Crossed Molecular Beam Scattering Technique. *J. Phys. Chem. A* **2008**, *112*, 1363-1379.
- 16 Leonori, F.; Skouteris, D.; Petrucci, R.; Casavecchia, P.; Rosi, M.; Balucani, N. Combined Crossed Beam and Theoretical Studies of the $C(^1D) + CH_4$ Reaction. *J. Chem. Phys.* **2013**, *138*, 024311.
- 17 Scott, D. C.; de Jaun, J.; Robie, D. C.; Schwartz-Lavi, D.; Reisler, H. Reactions of $C(^1D)$ with H_2 and HCl : Product State Excitations, Λ -Doublet Propensities and Branching Ratios. *J. Phys. Chem.* **1992**, *96*, 2509-2518.
- 18 Shannon, R. J.; Cossou, C.; Loison, J.-C.; Caubet, P.; Balucani, N.; Seakins, P. W.; Wakelam, V.; Hickson, K. M. The Fast $C(^3P) + CH_3OH$ Reaction as an Efficient Loss Process for Gas-Phase Interstellar Methanol. *RSC Adv.* **2014**, *4*, 26342–26353.
- 19 Hickson, K. M.; Loison, J.-C.; Guo, H.; Suleimanov, Y. V. Ring-Polymer Molecular Dynamics for the Prediction of Low-Temperature Rates: An Investigation of the $C(^1D) + H_2$ Reaction. *J. Phys. Chem. Lett.* **2015**, *6*, 4194-4199.
- 20 Grondin, R.; Loison, J.-C.; Hickson, K. M., Low Temperature Rate Constants for the Reactions of $O(^1D)$ with N_2 , O_2 and Ar, *J. Phys. Chem. A* **2016**, DOI: 10.1021/acs.jpca.5b12358.
- 21 Donovan, R. J.; Husain, D. Recent Advances in the Chemistry of Electronically Excited Atoms. *Chem. Rev.* **1970**, *70*, 489.

- 22 Davidson, J. A.; Schiff, H. I.; Brown, T. J.; Streit, G. E.; Howard C. J. Rate Constants for the Deactivation of O(¹D) by Xe, Kr, and Ar Over the Range 110–330 K. *J. Chem. Phys.* **1978**, *69*, 1213-1215.
- 23 Streit, G. E.; Howard, C. J.; Schmeltekopf, A. L.; Davidson, J. A.; Schiff, H. I. Temperature-Dependence of O(¹D) Rate Constants for Reactions with O₂, N₂, CO₂, O₃, and H₂O. *J. Chem. Phys.* **1976**, *65*, 4761-4764.
- 24 Blitz, M. A.; Dillon, T. J.; Heard, D. E.; Pilling M. J.; Trought, I. D. Laser Induced Fluorescence Studies of the Reactions of O(¹D₂) with N₂, O₂, N₂O, CH₄, H₂, CO₂, Ar, Kr and n-C₄H₁₀. *Phys. Chem. Chem. Phys.* **2004**, *6*, 2162-2171.
- 25 Defazio, P.; Gamallo, P.; Petrongolo, C. Nonadiabatic Dynamics of O(¹D) + N₂(X¹Σ_g⁺) --> O(³P) + N₂(X¹Σ_g⁺) on Three Coupled Potential Surfaces: Symmetry, Coriolis, Spin-Orbit, and Renner-Teller Effects. *J. Chem. Phys.* **2012**, *136*, 054308.
- 26 Gao, H.; Song, Y.; Chang, Y.-C.; Shi, X.; Yin, Q.-Z.; Wiens, R. C.; Jackson, W. M.; Ng, C. Y. Branching Ratio Measurements for Vacuum Ultraviolet Photodissociation of ¹²C¹⁶O. *J. Phys. Chem. A* **2013**, *117*, 6185–6195.
- 27 Hebrard, E.; Dobrijevic, M.; Loison, J.-C.; Bergeat, A.; Hickson, K. M.; Caralp, F. Photochemistry of C₃H_p Hydrocarbons in Titan's Stratosphere Revisited. *Astron. Astrophys.* **2013**, *552*, A132.
- 28 Braun, W.; Bass, A. M.; Davis, D. D.; Simmons, J. D. Flash Photolysis of Carbon Suboxide: Absolute Rate Constants for Reactions of C(³P) and C(¹D) with H₂, N₂, CO, NO, O₂ and CH₄. *Proc. Roy. Soc. A* **1969**, *312*, 417-434.

29 Husain, D.; Kirsch, L. J. The Study of Electronically Excited Carbon Atoms, C(2¹D₂), by Photoelectric Measurement of Time-Resolved Atomic Absorption. *Chem. Phys. Lett.* **1971**, *9*, 412-415.

30 Rowe, B. R.; Dupeyrat, G.; Marquette, J. B.; Gaucherel, P. Study of the Reactions N₂⁺ + 2 N₂ → N₄⁺ + N₂ and O₂⁺ + 2 O₂ → O₄⁺ + O₂ from 20 to 160 K by the CRESU Technique. *J. Chem. Phys.* **1984**, *80*, 4915-4921.

31 Daugey, N.; Caubet, P.; Bergeat, A.; Costes, M.; Hickson, K. M. Reaction Kinetics to Low Temperatures. Dicarbon + Acetylene, Methylacetylene, Allene and Propene from 77 ≤ T ≤ 296 K. *Phys. Chem. Chem. Phys.* **2008**, *10*, 729–737.

32 Hickson, K. M.; Bergeat, A. Low Temperature Kinetics of Unstable Radical Reactions. *Phys. Chem. Chem. Phys.* **2012**, *14*, 12057-12069.

33 Bourgalais, J.; Capron, M.; Kailasanathan, R. K. A.; Osborn, D. L.; Hickson, K. M.; Loison, J.-C.; Wakelam, V.; Goulay, F.; Le Picard, S. D. The C(³P) + NH₃ Reaction in Interstellar Chemistry: I. Investigation of the Product Formation Channels. *Astrophys. J.* **2015**, *812*, 106.

34 Hickson, K. M.; Loison, J.-C.; Bourgalais, J.; Capron, M.; Le Picard, S. D.; Goulay, F.; Wakelam, V. The C(³P) + NH₃ Reaction in Interstellar Chemistry: II. Low Temperature Rate Constants and Modeling of NH, NH₂ and NH₃ Abundances in Dense Interstellar Clouds. *Astrophys. J.* **2015**, *812*, 107.

35 Husain, D.; Newton D. P. Collisional Quenching of Electronically Excited Carbon Atoms, C[2p²(¹S₀)]. *J. Chem. Soc. Faraday Trans. 2*, **1982**, *78*, 51-71.

- 36 Husain, D.; Kirsch, L. J. Study of Electronically Excited Carbon Atoms, $C(2^1D_2)$, by the Attenuation of Atomic Emission, ($3^1P_1 \rightarrow 2^1D_2$). Part 1.—Collisional Deactivation of $C(2^1D_2)$ by the Noble Gases. *Trans. Faraday Soc.*, **1971**, *67*, 2886-2895.
- 37 Shiozaki, T.; Knizia, G.; Werner, H.-J. Explicitly Correlated Multireference Configuration Interaction: MRCI-F12. *J. Chem. Phys.* **2011**, *134*, 034113.
- 38 Werner H.-J.; Knowles, P. J. An Efficient Internally Contracted Multiconfiguration–Reference Configuration Interaction Method. *J. Chem. Phys.* **1988**, *89*, 5803-5814.
- 39 Langhoff, S. R.; Davidson, E. R. Configuration Interaction Calculations on the Nitrogen Molecule. *Int. J. Quantum Chem.* **1974**, *8*, 61-72.
- 40 Werner, H.-J.; Knowles, P. J.; Knizia, G.; Manby, F. R.; Schütz, M. WIREs. *Comput. Mol. Sci.* **2012**, *2*, 242-253.
- 41 MOLPRO is a package of *ab initio* programs written by H.-J. Werner, P. J. Knowles, G. Knizia, F. R. Manby, M. Schütz, P. Celani, T. Korona, R. Lindh, A. Mitrushenkov, G. Rauhut, et al.
- 42 Berning, A.; Schweizer, M.; Werner, H.-J.; Knowles, P. J.; Palmieri, P. Spin-Orbit Matrix Elements for Internally Contracted Multireference Configuration Interaction Wavefunctions, *Mol. Phys.* **2000**, *98*, 1823-1833.
- 43 Clifford, E. P.; Wenthold, P. G.; Lineberger, W. C.; Petersson, G. A.; Broadus, K. M.; Kass, S. R.; Kato, S.; DePuy, C. H.; Bierbaum, V. M.; Ellison, G. B. Properties of Diazocarbene [CNN] and the Diazomethyl Radical [HCNN] via Ion Chemistry and Spectroscopy,” *J. Phys. Chem. A* **1998**, *102*, 7100–7112.

44 Pd, R.; Chandra, P. Ground and Valence Excited States of C₂N and CN₂ Transients: Ab Initio Geometries, Electronic Structures, and Molecular Properties,” *J. Chem. Phys.* **2001**, *114*, 1589–1600.

45 Dagdigian, P. J.; Alexander, M. H.; Kłos, J. Theoretical Investigation of the Dynamics of O(¹D → ³P) Electronic Quenching by Collision with Xe. *J. Chem. Phys.* **2015**, *143*, 054306.

46 HIBRIDON is a package of programs for the time-independent quantum treatment of inelastic collisions and photodissociation written by M. H. Alexander, D. E. Manolopoulos, H.-J. Werner, B. Follmeg, P. J. Dagdigian, and others. More information and/or a copy of the code can be obtained from the website <http://www2.chem.umd.edu/groups/alexander/hibridon>.

47 Lanza, M.; Kalugina, Y.; Wiesenfeld, L.; Lique, F. Near-Resonant Rotational Energy Transfer in HCl–H₂ Inelastic Collisions. *J. Chem. Phys.* **2014**, *140*, 064316.

48 Garofalo, L. A.; Smith, M. C.; Dagdigian, P. J.; Kłos, J.; Alexander, M. H.; Boering, K. A.; Lin, J. J. Electronic Quenching of O(¹D) by Xe: Oscillations in the Product Angular Distribution and their Dependence on Collision Energy. *J. Chem. Phys.* **2015**, *143*, 054307.